International Journal of Minerals, Metallurgy and Materials
Volume 27, Number 4, April 2020, Page 526
https://doi.org/10.1007/s12613-019-1931-5

Effect of chemical activation process on adsorption of As(V) ion from aqueous solution by mechano-thermally synthesized zinc ferrite nanopowder

Mohammad Sefidmooy Azar, Shahram Raygan, and Saeed Sheibani

School of Metallurgy and Materials Engineering, College of Engineering, University of Tehran, Tehran, Iran

(Received: 30 May 2019; revised: 4 October 2019; accepted: 16 October 2019)

Abstract: Nanostructured $ZnFe_2O_4$ was synthesized by the heat treatment of a mechanically activated mixture of ZnO/α-Fe_2O_3. X-ray diffraction (XRD) and differential thermal analysis (DTA) results demonstrated that, after 5 h of the mechanical activation of the mixture, $ZnFe_2O_4$ was formed by heat treatment at 750°C for 2 h. To improve the characteristics of $ZnFe_2O_4$ for adsorption applications, the chemical activation process was performed. The 2 h chemical activation with 1 mol·L^{-1} HNO_3 and co-precipitation of 52%–57% dissolved $ZnFe_2O_4$ led to an increase in the saturated magnetization from 2.0 to 7.5 emu·g^{-1} and in the specific surface area from 5 to 198 $m^2 \cdot g^{-1}$. In addition, the observed particle size reduction of chemically activated $ZnFe_2O_4$ in field emission scanning electron microscopy (FESEM) micrographs was in agreement with the specific surface area increase. These improvements in $ZnFe_2O_4$ characteristics considerably affected the adsorption performance of this adsorbent. Adsorption results revealed that mechano-thermally synthesized $ZnFe_2O_4$ had the maximum arsenic adsorption of 38% with the adsorption capacity of 0.995 mg·g^{-1} in a 130 mg·L^{-1} solution of As(V) after 30 min of agitation. However, chemically activated $ZnFe_2O_4$ showed the maximum arsenic adsorption of approximately 99% with the adsorption capacity of 21.460 mg·g^{-1} under the same conditions. These results showed that the weak adsorption performance of mechano-thermally synthesized $ZnFe_2O_4$ was improved by the chemical activation process.

Keywords: zinc ferrite; mechano-thermal; chemical activation; adsorption; arsenic(V)

1. Introduction

Currently, the increasing use of heavy metals in different industries has become a global environmental concern for water pollution because of industrial wastewaters. Arsenic is a toxic heavy metal that enters water sources via the wastewater from industries that produce metals, pigments, textiles, paper, and metal adhesives [1]. Nervous system problems, dermal system diseases, diabetes, cardiovascular system diseases, and hematological problems may be caused by prolonged exposure to polluted arsenic-containing water and foods [2]. Based on various studies, the adsorption process has a cost-effective, efficient, and fast performance for the removal of heavy metals from aqueous solutions compared with other routine techniques such as chemical precipitation, ion exchange, reverse osmosis, coagulation, and flocculation, membrane filtration, and electrochemical removal [3]. Magnetic nanostructured adsorbents, such as magnetite and ferrites, have attracted considerable attention in heavy metal adsorption studies because magnetic absorbent can be separated from aqueous solutions by an external magnetic field [4]. The superior characteristics of ferrites have resulted in considerable attention to them as efficient adsorbents for heavy metal removal from aqueous solutions. Tu *et al.* [5] employed the hydrothermal method to prepare zinc ferrite nanoparticles with high efficiency for the Mo(VI) removal/recovery process from water. Various studies have been conducted on arsenic adsorption with chemically synthesized ferrites. As(III) and As(V) removal by different adsorbents (e.g., Fe_3O_4, Mn_2O_3, and hydrothermally synthesized manganese ferrite [6]), the removal of these anions by co-precipitated manganese ferrite nanoparticles [7], and As(III) adsorption on microwave hydrothermally synthesized cobalt and manganese ferrite [8] have been reported.

Mechanical activation and chemical methods are the most prevalent routes for ferrite synthesis. Based on various

Corresponding author: Shahram Raygan E-mail: shraygan@ut.ac.ir

studies, chemically synthesized ferrites produced by different methods (e.g., co-precipitation, sol–gel, hydrothermal, solvothermal, and thermal composition) have superior adsorption performance compared to mechanically or mechano-thermally prepared ferrites; this difference is attributed to the higher distribution homogeneity, higher specific surface area, and lower agglomeration of ferrite particles synthesized by chemical routes [9–11]. Adsorption is a surface reaction that is controlled by the number of active sites on the surface of adsorbents. Higher specific surface results in more active sites and better adsorption efficiency. Druska *et al.* [9] prepared zinc ferrite by the mechano-thermal method with the specific surface of 10.9 $m^2 \cdot g^{-1}$. Based on various studies chemically synthesized ferrites usually have higher specific surfaces. These approaches include hydrothermally synthesized cobalt ferrite with 85.4 $m^2 \cdot g^{-1}$ [12], co-precipitated manganese ferrite with 180.0 $m^2 \cdot g^{-1}$ [10], and solvothermally synthesized zinc ferrite with 70.0 $m^2 \cdot g^{-1}$ [13] specific surface areas. Because of the low specific surface area, mechanically, or mechano-thermally synthesized ferrites are rarely used for heavy metal adsorption. However, Hosseinzadeh *et al.* [14] prepared magnetite by 45 h of mechanical milling of Fe_2O_3 in an argon atmosphere. The synthesized magnetite showed the adsorption capacity of approximately 12 $mg \cdot g^{-1}$ for Pb^{2+} and 11 $mg \cdot g^{-1}$ for Cd^{2+} ions. This mechanically synthesized magnetite had an inferior performance compared to co-precipitated magnetite with the adsorption capacity of 52.9 $mg \cdot g^{-1}$ for Pb^{2+} [15] and 35.46 $mg \cdot g^{-1}$ for Cd^{2+} in the presence of other ions [16].

The chemical activation process may be useful for improving the adsorption efficiency of ferrites but the effect of this process on ferrites is unknown. However, the process is widely used to improve the red mud specific surface area and chemical composition [17]. The chemical activation process by different acids partially dissolves red mud particles, which is accompanied by surface cavity formation and an increase in the specific surface of red mud. Furthermore, by adding an alkaline agent after chemical activation in the acidic solution, the pH value in the precipitation zone of dissolved compounds increases, and particles with a higher specific surface area, and lower size distribution are reformed. Sahu *et al.* [18] used HCl-treated red mud for Pb^{2+} removal from water. They reported a considerable decrease in the particle size and an increase in the specific surface area from 33.50 to 67.10 $m^2 \cdot g^{-1}$ owing to the acid treatment, which led to better adsorption performance. It is well-known that red mud contains various metal oxides such as Fe_2O_3, Al_2O_3, SiO_2, and TiO_2 [19]. Therefore, the chemical activation process may be useful for improving the effective adsorption characteristics of ferrites owing to their similar metal oxide nature. Another process for the chemical activation of ferrites is to use H_2SO_4, HNO_3, and HCl for the acid treatment of ternary oxide of $LiMnO_2$ (which has a spinel structure similar to that of ferrites) to prepare MnO_2, as reported by Hunter [20]. These researchers reported that the acid treatment separated alkali ions from the spinel structure. In addition, the partial dissolution of resultant MnO_2 and its re-precipitation produced finer particles with higher homogeneity. Thus, this effect may be also observed in ferrite.

The effect of the chemical activation process on ferrites has not been investigated yet. Thus, the main goal of this study is to chemically activate mechano-thermally synthesized zinc ferrite for the first time. In the second step, the evaluation of chemical activation effect on zinc ferrite characteristics (e.g., surface area, saturated magnetization, and particle distribution) will be investigated. The final step will be to study the zinc ferrite performance for adsorbing As(V) ions from a simulated acidic wastewater.

2. Experimental

To synthesize the zinc ferrite powder, high-energy ball milling was performed on a mixture of ZnO and α-Fe_2O_3 (Merck, 99% purity) with a molar ratio of 1:1 (mass ratio of 1:2) as starting materials in air for 5 h in a planetary ball mill (Model PM2400, Asia Sanaat Rakhsh, Iran) with the rotation speed of 300 r/min and the ball-to-powder mass ratio of 20:1. Moreover, 4, 8, and 10 hardened steel balls with 19, 13, and 8 mm diameters were utilized in a 300 mL hardened steel vial for ball milling. The milling process was stopped for 15 min in 1 h intervals to prevent the temperature increase in vials. Next, 180 mg of stearic acid (Sigma, 98% purity) and 9 g of the ZnO and α-Fe_2O_3 mixture was used as the process control agent during milling to avoid the agglomeration of powders. Differential thermal analysis (DTA) was performed on non-activated and 5 h activated mixtures using an STA 504-Bahr thermal analysis system with the heating rate of 40°C·min^{-1} to determine the final temperature of the reaction in mixtures. The un-milled and milled powders were heat-treated at DTA-determined temperatures for 2 h in an ATRA PC-15 furnace to synthesize a nanocrystalline zinc ferrite powder. To chemically activate synthesized zinc ferrite, 200 mg of zinc ferrite was acid treated with 200 mL of 1, 2, and 3 mol/L nitric acid for 2 h at 80°C. Subsequently, the solution was added dropwise into 200 mL of a high-concentration NaOH solution at 80°C to re-precipitate zinc ferrite from Fe and Zn ions that exist in

the acid treatment solution. To complete the re-precipitation of zinc ferrite, the final solution was stirred for 1 h at 80°C. After the magnetic solid-liquid separation of chemically activated zinc ferrite with a 0.45 T magnet, the final powder was washed with deionized water and dried at 70°C within 15 h.

The structural characteristics of various samples were studied by X-ray diffraction (XRD) using a Philips PW3040/60 X-ray diffractometer at 40 kV and 100 mA with a Cu K_α radiation. The microstructural characterization was performed via field-emission scanning electron microscopy (FESEM) using a MIRA3 TESCAN instrument. The ImageJ software was applied to calculate the average particle size of powders via the image analysis method based on FESEM micrographs; the reported numbers are the average of 20−30 measurements for different samples. The specific surface area of samples was determined by a BEL-Belsorp II instrument with nitrogen adsorption at 77 K based on Brunauer-Emmett-Teller (BET) isotherm. Moreover, a vibrating sample magnetometer (Meghnatis Daghigh Kavir Co., Iran) was used to study the magnetic characteristics of samples at room temperature. In addition, Fourier Transform Infrared (FTIR) spectroscopy (ThermoElectron, model AVATAR, USA) was used to determine the chemical activation effect on the adsorbent.

Both mechano-thermally synthesized zinc ferrite (hereafter called the MTZF sample) and chemically activated zinc ferrite (hereafter called the CAZF sample) were evaluated as the adsorbents of As(V) from simulated industrial wastewater. All adsorption experiments were conducted using the batch method. Thus, 130 mg·L^{-1} of As(V) and 4000 mg·L^{-1} of SO_4^{2-} solutions were simulated according to the chemical analysis of wastewater from the copper extraction industry and used as the polluted solution for adsorption experiments. The pH value in all experiments was adjusted to 3 to be close to wastewater intrinsic pH and achieve good electrostatic attraction between As(V) anions and ferrite surfaces in highly acidic solutions [11,21−22]. Furthermore, 20 mL of simulated wastewater, 5, 10, 20, 30, 40, and 50 g·L^{-1} of MTZF, and 1, 2, 3, 4, 5, and 6 g·L^{-1} of CAZF were stirred for 30 min to investigate the effect of adsorbent dosage on As(V) adsorption. The effect of stirring time on As(V) adsorption was studied by stirring 20 mL of simulated wastewater with 1 g of MTZF and 0.1 g of CAZF for 5−120 min. After each experiment, the adsorbent was magnetically separated from the liquid phase using a 0.45 T magnet and filtration. The As(V) concentration in the remaining solutions was determined by the ICP-OES (VARIAN VISTA-PRO, Optima7300DV) method with a detection limit of 50 μg·L^{-1} for arsenic ions. The adsorption capacity and As(V) removal percent were calculated using the difference between the initial and final As(V) concentrations.

3. Results and discussion

The XRD patterns of un-milled and milled samples are shown in Fig. 1. The pattern of the un-milled mixture shows the peaks of α-Fe_2O_3 (JCPDS file number 01-085-0599) and ZnO (JCPDS file number 01-075-0576) phases only, while some of α-Fe_2O_3 and most peaks of ZnO disappeared for the milled mixture. The pattern of the milled sample showed an increase in the peak width and a decrease in the diffraction intensities owing to the amorphous nature of the milled mixture. Furthermore, peak broadening after ball milling may be due to a decrease in the crystallite size and an increase in the internal lattice strains. These parameters for both samples were calculated based on α-Fe_2O_3 via the Williamson-Hall method [23]. After 5 h of ball milling, the average crystallite size decreased from 139 to 25 nm, and the lattice strain increased from 0.09% to 0.41%. In addition, three integrated peaks in the 2θ range of 35°−38°, 56°−59°, and 62°−65° were observed in this sample. The three major peaks of $ZnFe_2O_4$ based on the JCPDS file (01-089-1011) are located at the diffraction angles of 35.280°, 62.243°, and 56.687°. According to the major peaks of $ZnFe_2O_4$, the integrated peaks in the milled sample pattern may be related to the beginning of the following mechano-chemical Reaction (1):

$$ZnO + Fe_2O_3 \rightarrow ZnFe_2O_4 \quad (1)$$

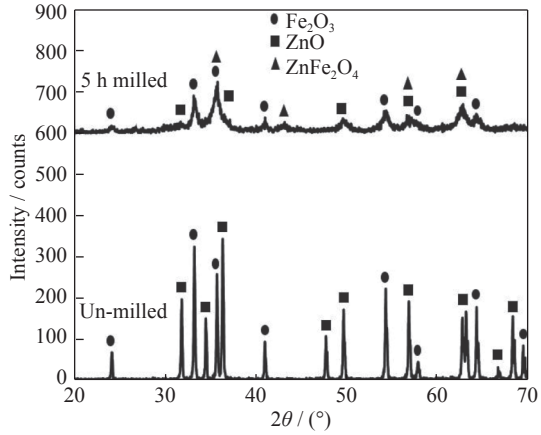

Fig. 1. XRD patterns of the un-milled and 5 h milled powder mixtures.

It is worth noting that other peaks of zinc ferrite may exist in the XRD pattern at very low intensities because of its more amorphous nature [24]. The presence of α-Fe_2O_3 and

ZnO peaks in the XRD pattern of milled sample proved that the formation reaction of $ZnFe_2O_4$ cannot be completed by 5 h of milling. It has been previously reported that prolonged milling times were required to complete the mechano-chemical reaction of ferrites under similar conditions [25−26].

Fig. 2 shows the FESEM micrographs of un-milled and milled samples. The morphology of the un-milled mixture is presented as a reference. In the 5 h milled sample, the primary shapes of starting materials changed into the agglomerates of fine particles made by ball mill grinding. It is clear that a considerable decrease in particle size occurred owing to milling. The heat treatment of un-milled and milled mixtures can be used to completely form nanocrystalline zinc ferrite. Required temperatures for the zinc ferrite formation reaction were determined based on DTA curves in Fig. 3 for both un-milled and milled powder mixtures. The DTA curve for the un-milled mixture demonstrated an exothermic peak with the onset and final temperatures of approximately 830°C and 1080°C, respectively. The onset and final peak temperatures for the 5 h milled mixture considerably decreased to 550°C and 730°C, respectively. It is clear that the DTA peak for the 5 h milled mixture had a shorter temperature range compared to the un-milled mixture, which indicated that the mechanical activation process improved the reaction kinetics and decreased the energy required for zinc ferrite formation owing to a decrease in the particle and crystallite size and an increase in the internal lattice strains after milling based on the FESEM micrographs and Williamson-Hall calculations. In addition, the exothermic peak in the temperature range of approximately 100−360°C belonged to the stearic acid decomposition reaction [27].

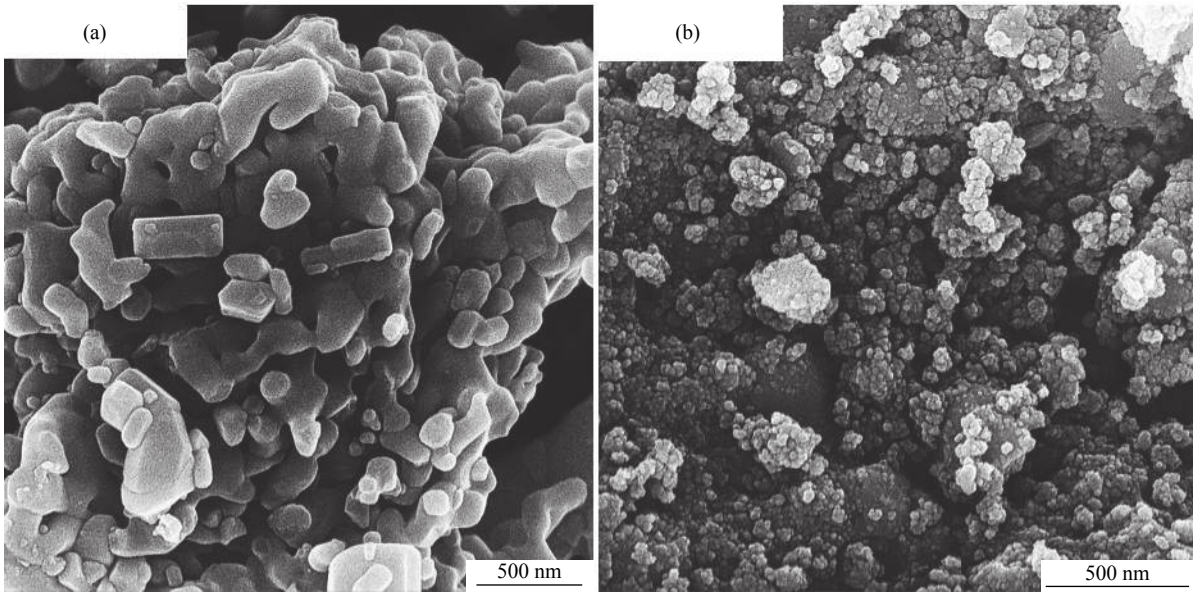

Fig. 2. FESEM micrographs for (a) un-milled and (b) 5 h milled samples.

The XRD patterns of heat-treated samples (Fig. 4) show the complete formation of zinc ferrite after the heat treatment (HT) of both un-milled and milled mixtures. The heat treatment temperatures were selected according to the DTA results. It is clear that the mechanical activation process resulted in the complete formation of zinc ferrite at 750°C, lower than the temperature of the un-milled primary mixture.

Fig. 5 shows the FESEM micrograph of the 5 h milled and heat-treated sample at 750°C (MTZF). It is clear that high agglomeration and particle growth are made by heat treatment compared with the milled sample (Fig. 2(b)). From a quantitative viewpoint, the average particle size for the 5 h milled and MTZF sample was calculated via the image analysis technique as 33 and 65 nm, respectively, showing a notable increase in the particle size owing to the heat treatment.

The specific surface area of the MTZF sample was measured by the BET method as 5 $m^2 \cdot g^{-1}$. It is reported in the literatures that the specific surface area of mechano-thermally synthesized ferrites usually has lower amounts compared with chemically synthesized ones [9−10]. Fig. 5 shows that the growth and high agglomeration of particles made by heat treatment in the MTZF sample negatively affected the specific surface area of ferrite. The adsorption process is highly dependent on available sites on the adsorbent surface. Thus, specific surface area is a very important

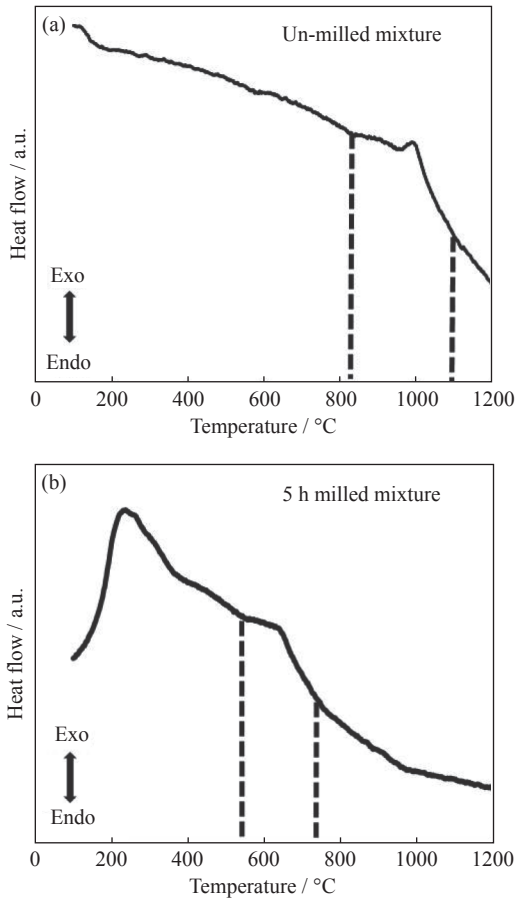

Fig. 3. DTA curves for (a) un-milled and (b) milled mixtures.

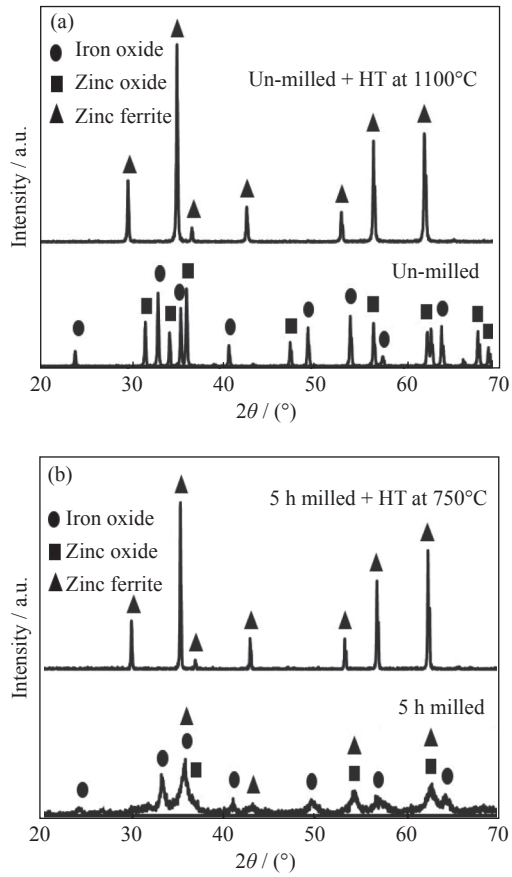

Fig. 4. XRD patterns of (a) un-milled and (b) 5 h milled powder mixtures before and after the heat treatment (HT) at different temperatures.

characteristic of an adsorbent that influences adsorption efficiency [10]. Based on these explanations, the low amount of MTZF specific surface area may be a negative parameter in this sample performance as an adsorbent. Therefore, chemical activation was used to improve the specific surface area of the produced MTZF powder.

The chemical activation process is accompanied by the acidic dissolution of zinc ferrite based on Reaction (2):

$$ZnFe_2O_4 + 8H^+ \rightarrow Zn^{2+} + 2Fe^{3+} + 4H_2O \quad (2)$$

The dissolution percentage of MTZF at various HNO_3 concentrations is observed in Fig. 6. Based on the dissolved Fe analysis, the leaching percentage after 2 h was calculated to be approximately 52%, 78%, and 83% for the HNO_3 concentrations of 1, 2, and 3 $mol \cdot L^{-1}$, respectively. On the basis of the dissolved Zn analysis, with a mild increase compared to the first calculation method, the leaching percentage was calculated to be approximately 57%, 79%, and 84% for the HNO_3 concentrations of 1, 2, and 3 $mol \cdot L^{-1}$, respectively. The observed difference between the leaching percentages calculated by the two methods is due to the partial conversion of aqueous Fe^{3+} to solid Fe_2O_3 (not detectable by the ICP-OES method) during the dissolution step based on Reaction (3) [28–29]. Therefore, it seems that dissolution percentage determination was more accurate based on dissolved Zn.

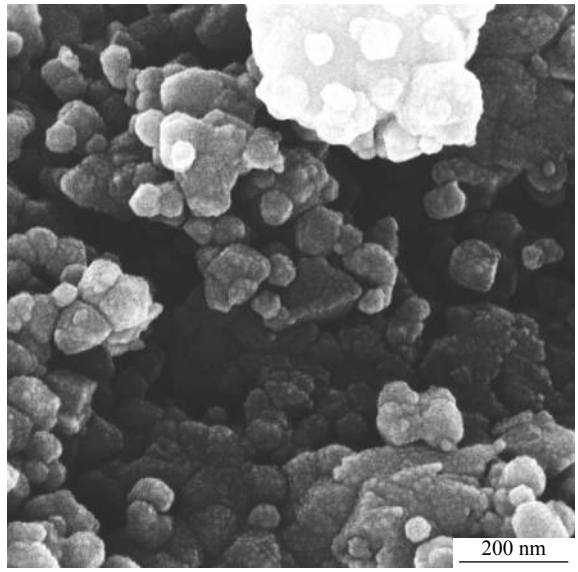

Fig. 5. FESEM micrograph of the MTZF sample.

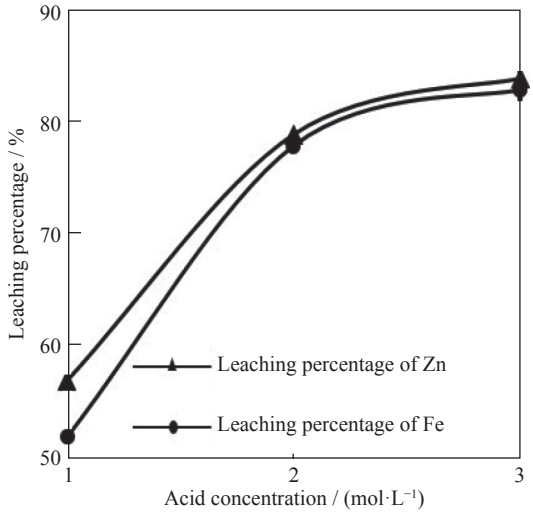

Fig. 6. Percentage of zinc ferrite leaching at various acid concentrations calculated on the basis of the amounts of dissolved Fe and Zn.

$$ZnFe_2O_4 + 2H^+ \rightarrow Zn^{2+} + Fe_2O_3 + H_2O \quad (3)$$

By adding the chemical activation solution to the high-concentration sodium hydroxide solution, zinc ferrite re-precipitated based on Reactions (4)–(6) [30–32]. During the pH increase, Fe_2O_3 (which was formed based on Reaction (3)) was converted to $Fe(OH)_3$, and this hydroxide reacted with zinc ferrite based on solid-state Reaction (6). Thus, Fe_2O_3 did not pose a problem for ferrite co-precipitation.

$$Zn^{2+} + 2Fe^{3+} + 8OH^- \rightarrow ZnFe_2O_4 + 4H_2O \quad (4)$$

$$Zn^{2+} + 2Fe^{3+} + 8OH^- \rightarrow Zn(OH)_2 + 2Fe(OH)_3 \quad (5)$$

$$Zn(OH)_2 + 2Fe(OH)_3 \rightarrow ZnFe_2O_4 + 4H_2O \quad (6)$$

It was predicted that chemical activation with more concentrated acid would lead to a final product with superior modified properties because more particles will be available for re-precipitation in the second step of the chemical activation process. However, the specific surface area unexpectedly decreased from 198 to 177, and 171 $m^2 \cdot g^{-1}$ for HNO_3 concentrations of 1, 2, and 3 $mol \cdot L^{-1}$, respectively. Chemical activation in more dilute acidic solution led to the re-precipitation of zinc ferrite with a higher specific surface area because of the higher supersaturation during precipitation with the high-concentration NaOH solution. If the difference between the concentrations of NaOH and HNO_3 is the cause of supersaturation during re-precipitation, it can be concluded that a higher supersaturation from 1 $mol \cdot L^{-1}$ HNO_3 was responsible for zinc ferrite formation with a higher specific surface area during the chemical activation process. It is known that at higher supersaturation conditions, nucleation rate will overcome the growth rate [33], and this phenomenon would lead to the formation of sediments with finer particles, higher homogeneity in distribution and, consequently, higher specific surface area. The FESEM images of chemically activated samples demonstrated in Fig. 7 confirmed the BET analysis results. Fig. 5(b) shows the agglomerated particles of MTZF as a comparison reference, and Figs. 7(a)–7(d) show the images of chemically activated ferrites. It is clear that the sample processed in 1 $mol \cdot L^{-1}$ HNO_3 (shown in Fig. 7(a)) has a finer and more homogenous particle distribution compared with chemically activated ferrite samples (shown in Figs. 7(c) and 7(d)) that were produced in 2 and 3 $mol \cdot L^{-1}$ HNO_3, respectively. The average particle sizes were calculated via the image analysis method as 23, 27, and 28 nm for 1, 2, and 3 $mol \cdot L^{-1}$ acid concentrations, respectively.

Fig. 7(b) shows another FESEM image of the chemically activated zinc ferrite with 1 $mol \cdot L^{-1}$ HNO_3 taken from another area of the sample. It is observed that the activated powder has a dual structure that includes mechano-thermal ferrite remaining from the previous steps and partially co-precipitated ferrite during the chemical activation process. In addition, this structure may be seen in other areas of samples that were chemically activated with 2 and 3 $mol \cdot L^{-1}$ acids. It is observed that the large agglomerated particles of mechano-thermal ferrite are located in marked areas, and the finer particles of new ferrite precipitated on the surface of MTZF particles. As explained in the previous paragraph, lower acid concentration resulted in better properties of final ferrite; however, further concentration reduction may increase the MTZF volume fraction, which has unfavorable microstructural and magnetic properties. The volume fraction of MTZF can be reduced to zero using an HNO_3 solution with a concentration greater than 3 $mol \cdot L^{-1}$. Thus, if it is possible to obtain desirable results using a more diluted acid, it is not logical to use high-concentration acids that cause health-related, environmental, and instrumental problems, especially near the boiling temperature. Therefore, to reach a balance between MTZF volume fraction, acceptable microstructural characteristics, and environmental considerations, chemically activated zinc ferrite in 1 $mol \cdot L^{-1}$ HNO_3 with an abbreviation of CAZF was chosen as the suitable adsorbent.

The XRD patterns of MTZF and CAZF samples are shown in Fig. 8. It is clear that the CAZF sample exhibits only zinc ferrite peaks. In addition, this sample has a more amorphous structure because of the precipitation during its synthesis route. Similar studies have noted the possibility of goethite or iron(III) hydroxide formation during the co-precipitation of ferrites [34–35]. Whereas in this study, owing to the low amount of possible impurities and based on the

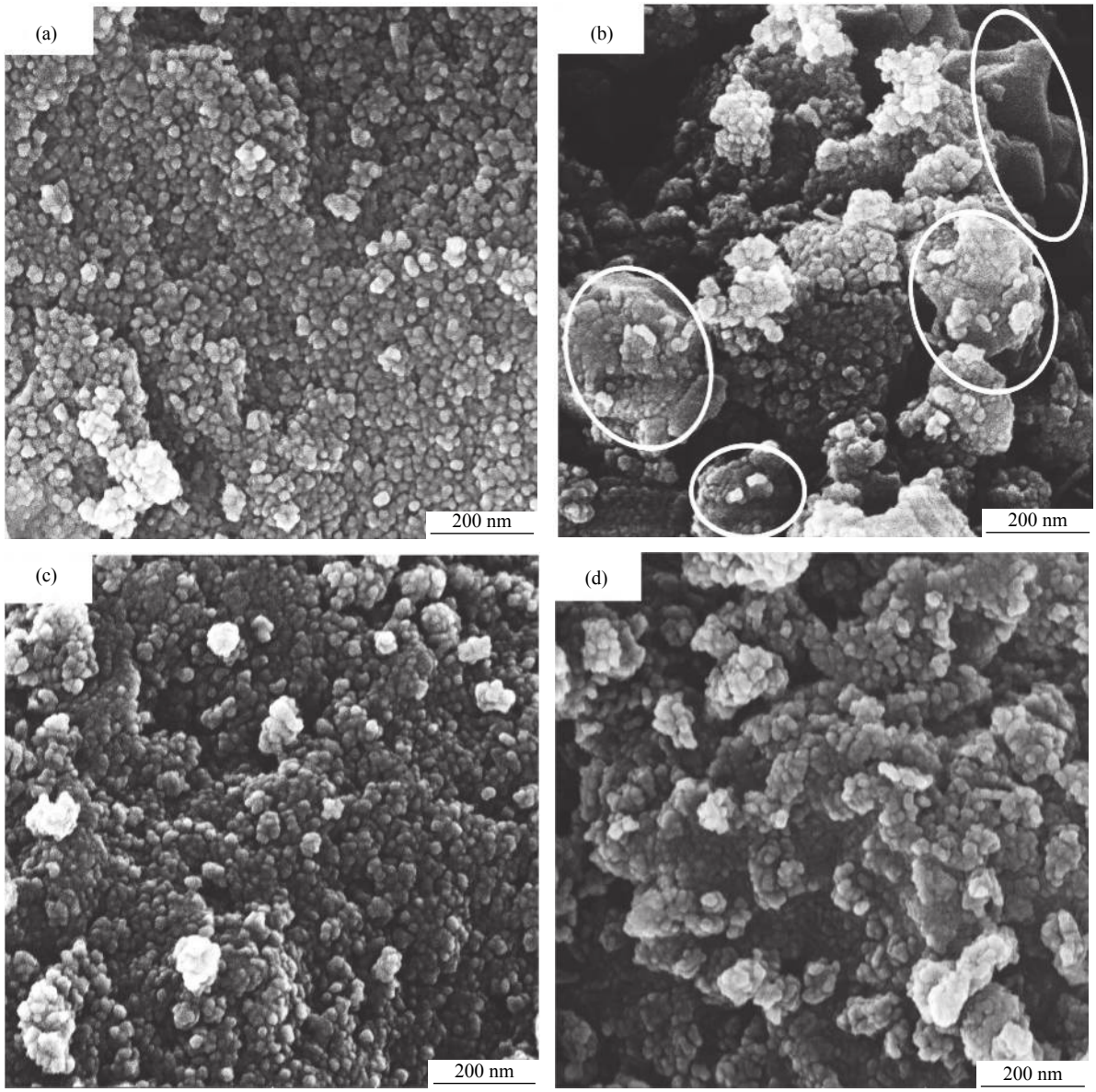

Fig. 7. FESEM micrographs of chemically activated ferrites in (a, b) 1 mol·L^{-1}, (c) 2 mol·L^{-1}, and (d) 3 mol·L^{-1} HNO_3.

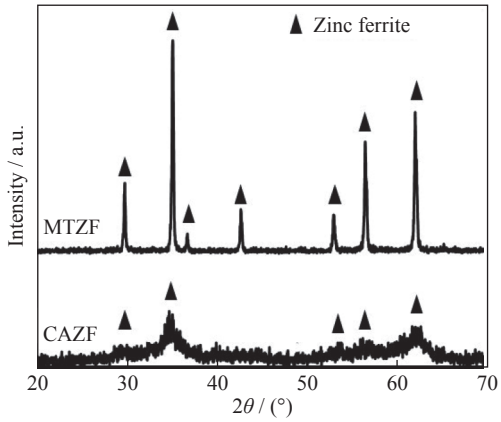

Fig. 8. XRD patterns of MTZF and CAZF samples.

XRD detection limit, there are no observable peaks related to goethite or iron(III) hydroxide. Moreover, the small degree of impurities may improve adsorption performance because of their strong heavy metal removal capability [36], especially for arsenic [37].

Fig. 9 shows the FTIR spectra of the MTZF and CAZF samples. The aim of this analysis was to investigate the possibility of the $Fe(OH)_3$/FeOOH formation during the chemical activation process because of uncertain XRD results that indicated that these Fe–OH bond-containing compounds were absent in the CAZF sample. Based on Fig. 9, it is clear that there is no notable difference between the two spectra, which indicates that both samples have the same nature and no new interaction is made in the zinc ferrite structure by the

chemical activation process. To identify Fe−OH interactions in the sample, the −OH vibration band had to be evaluated. There was a broad peak in the range of 3000−3700 cm^{-1}, and this approximate wave number range has been attributed to the −OH stretching vibration [38−39]. The comparison of MTZF and CAZF spectra in this wavenumber range confirmed that electrostatic interactions owing to chemical activation affected the −OH bands. Besides, the band at 3686 cm^{-1} was identified by Kefirov *et al.* [40] as the −OH stretching vibration peak, and both MTZF and CAZF adsorbents exhibited a similar band at that wavenumber. Kefirov *et al.* [40] claimed that the peaks at 1380 and 1400 cm^{-1} were attributed to Fe−OH and $-FeOH_2^+$ ligands, respectively. The spectra of CAZF demonstrated no movement or interaction in the mentioned wavenumber ranges compared with those in MTZF spectra. Therefore, the chemical activation process successfully re-produced zinc ferrite with modified characteristics, and the formed $Fe(OH)_3$/FeOOH during this step was negligible.

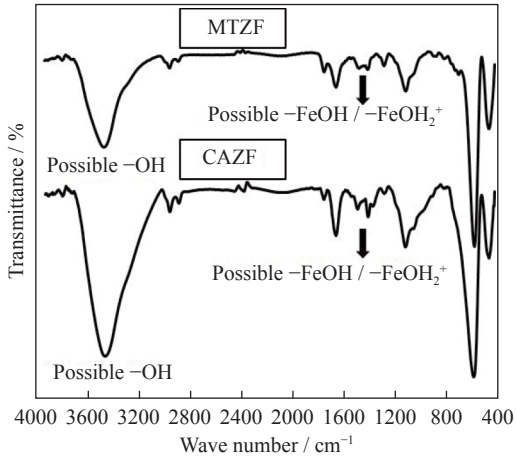

Fig. 9. FTIR spectra of MTZF and CAZF samples.

During the adsorption process, solid-liquid separation is a challenging step for non-magnetic nanostructured adsorbents [4]. If the adsorbent has acceptable magnetic properties, the solid-liquid separation can be performed by an external magnetic field [41]. Therefore, the magnetic properties of MTZF and CAZF adsorbents were measured by the vibrating sample magnetometer (VSM) method. The results of this experiment are shown in Fig. 10. It is clear that, by applying a 10000 Oe magnetic field, the magnitude of MTZF magnetization reached approximately 2.0 emu·g^{-1} but it did not become saturated. In addition to the small degree of magnetization, the small hysteresis loop also showed the weak magnetic properties of MTZF. The transition from inverse to normal spinel structure owing to the heat treatment [26,42−43] and the possible presence of antiferromagnetic Fe_2O_3 with a low magnetization of 0.4 emu·g^{-1} [44] in amounts lower than the XRD detection limit [45] are the reasons for the weak magnetic properties of MTZF. The undesirable magnetic characteristics of MTZF disrupted the magnetic separation process. Furthermore, the small amount of specific surface area and high agglomeration of MTZF particles had a weakening effect on the adsorption efficiency of this adsorbent. Consequently, the chemical activation process was applied to improve the adsorption performance of mechano-thermally synthesized zinc ferrite. Similar to MTZF, the CAZF sample showed unsaturated magnetization owing to the volume fraction of MTZF and $FeOOH/Fe(OH)_3$ impurities (even in low amounts) that have weak magnetic properties [46]. Nevertheless, compared to MTZF, the amount of saturation magnetization (M_s) increased to approximately 7.5 emu·g^{-1} in the working magnetic field range, and a larger hysteresis loop was observed. The improvement of magnetic properties after chemical activation is attributed to the reduction of particle size. The large surface-to-volume ratio in nanostructured particles can apply a noticeable strain on surface structure, which results in a decrease in the energy difference between tetrahedral and octahedral sites, promotes the change in cation distribution through the displacement of Zn^{2+} and Fe^{3+} between those sites, and creates inversion in the spinel structure of ferrite [26,47].

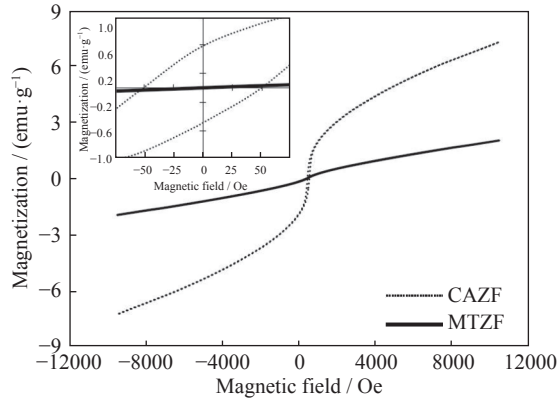

Fig. 10. Magnetization curves at room temperature for MTZF and CAZF samples (inset is the enlarged hysteresis loop for MTZF and CAZF samples).

The adsorption performance of both MTZF and CAZF adsorbents was investigated by the removal efficiency of As(V) from simulated acidic wastewater. Fig. 11 compares the removal efficiency of As(V) by various dosages (defined as S/L = the quality of adsorbent (S) in g/the volume of solution (L) in L) of MTZF and CAZF. These experiments were conducted at the solution concentration of 130 mg·L^{-1} As(V) and 30 min agitation time. Fig. 11(a) shows that for

the MTZF adsorbent at S/L = 5 g·L^{-1}, only approximately 5% of ions was removed. By increasing the MTZF dosage to S/L = 50 g·L^{-1}, the As(V) removal percentage finally reached approximately 38% with the adsorption capacity of 0.995 mg·g^{-1}. By increasing the MTZF dosage to S/L = 50 g·L^{-1}, no gradient drop was observed in Fig. 11(a). This means that the adsorption process did not reach saturation level possibly owing to the significant constraint in MTZF surface active sites because of the low specific surface area, which makes the adsorbent-ions contact very difficult. During adsorption, it is possible that all of the active sites of MTZF are occupied by arsenic ions. Even if some sites are not occupied, the insufficient adsorbent-ions contact leads to very slow kinetics, under this condition, a considerable fraction of ions cannot be removed after 30 min of agitation. By increasing agitation time, an enhancement in adsorption capacity may be achievable [48−49]. Compared to MTZF, the CAZF adsorbent had a considerably more efficient adsorption performance. Fig. 11(b) shows that for CAZF, approximately 59% of arsenic ions was removed in the dosage of S/L = 1 g·L^{-1}. By increasing dosage, a noticeable improvement in adsorption capacity is observed. Thus, at S/L = 5 g·L^{-1}, approximately 98%, and at S/L = 6 g·L^{-1}, more than 99% of arsenic ions were adsorbed. At the best removal percentage, the adsorption capacity of CAZF increased to 21.460 mg·g^{-1}. These results show the superior performance of this adsorbent compared to that of MTZF and, consequently, the impressive positive effect of the chemical activation process on the adsorption characteristics of zinc ferrite, which is related to a considerable increase in the specific surface area and a decrease in the particle size after the activation based on and FESEM micrographs (Figs. 5 and 7) and BET results.

The effect of agitation time on the adsorption behavior of MTZF and CAZF samples is demonstrated in Fig. 12. The results confirm the considerable enhancement in adsorption efficiency owing to the specific surface area and particle size improvement made by the chemical activation process. Fig. 12(a) shows that during the first 10 min, approximately 15% of arsenic ions was removed by 50 g·L^{-1}

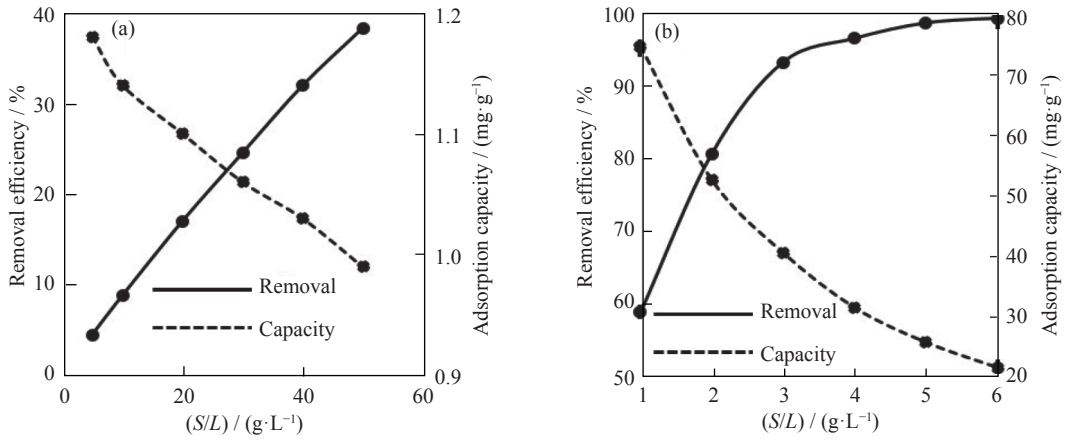

Fig. 11. Effect of adsorbent dosage on the adsorption efficiency of (a) MTZF and (b) CAZF.

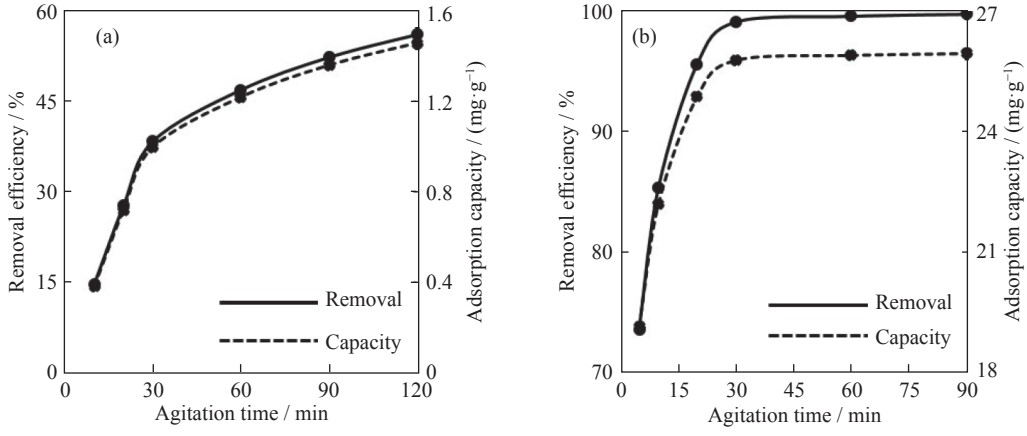

Fig. 12. Effect of agitation time on the adsorption efficiency by (a) 50 g·L^{-1} of MTZF and (b) 5 g·L^{-1} of CAZF.

of MTZF. By performing experiments up to 30 min, the removal percentage was increased with a constant slope to approximately 38%. The more prolonged tests were accompanied by a gradient drop, which indicated slower kinetics. The observed gradient drop and decrease in adsorption rate were not accompanied by an increase to the equilibrium state. Thus, noticeable parts of active sites were occupied by arsenic ions, which suggests that the diffusion of ions from the solution into adsorption sites was difficult [50]; however, a decrease in the adsorption rate was caused by the longer diffusion path of the ferrite surface [51], which made the adsorbent-ions contact very difficult. Finally, the removal percentage of approximately 56% and the adsorption capacity of approximately 1.453 $mg \cdot g^{-1}$ were achieved during the most prolonged experiment, i.e., 120 min of agitation. For CAZF, 5$g \cdot L^{-1}$ of this adsorbent successfully removed approximately 73% of arsenic ions in only 5 min. By increasing the agitation time up to 20 and 30 min, the removal percentage reached approximately 95% and 99%, respectively; then, more than 99% of arsenic ions were adsorbed on CAZF. The adsorption capacity of CAZF under the best conditions increased to approximately 25.875 $mg \cdot g^{-1}$. This performance confirmed the phenomenal improvement in the zinc ferrite adsorption efficiency owing to the chemical activation process. These results introduce chemical activation as a novel efficient process for the improvement of magnetic and microstructural characteristics in mechano-thermally synthesized ferrites or other metallic oxides.

4. Conclusion

Nanostructured zinc ferrite was successfully synthesized by the mechano-thermal method. Based on the DTA results, zinc ferrite was formed in the temperature range of 550−730°C by 5 h of mechanical activation of the ZnO and α-Fe_2O_3 mixture, while the formation reaction of zinc ferrite from un-milled ZnO and α-Fe_2O_3 mixture was completed in the temperature range of 830−1080°C. XRD results confirmed that DTA-derived temperatures were efficient at zinc ferrite synthesis. It is clear that mechanical activation considerably moderated the synthesis process including temperature and heat energy. FESEM showed high agglomeration in mechano-thermal zinc ferrite. The specific surface area of this ferrite was 5 $m^2 \cdot g^{-1}$ owing to agglomeration, and the saturated magnetization of this sample was 2.0 $emu \cdot g^{-1}$. These properties resulted in a weak adsorption performance of mechano-thermal zinc ferrite. The BET analysis showed that chemical activation with 1, 2, and 3 $mol \cdot L^{-1}$ HNO_3 acid decreased specific surface values from 198 to 177 and 171 $m^2 \cdot g^{-1}$, respectively. The more dilute acid exhibited better specific surface area owing to higher supersaturation during re-precipitation, which allows using the method with lower risk and environmental issues. Hence, chemically activated zinc ferrite with 1 $mol \cdot L^{-1}$ HNO_3 was chosen as the second adsorbent. Compared to the mechano-thermally synthesized sample, higher saturated magnetization (7.5 $emu \cdot g^{-1}$) and more homogenous and fine particle distribution were observed in the chemically activated sample. Adsorption results showed that 50 $g \cdot L^{-1}$ mechano-thermally synthesized sample achieved the maximum arsenic removal percentage of approximately 38% with the adsorption capacity of 0.995 $mg \cdot g^{-1}$ in 30 min. However, 6 $g \cdot L^{-1}$ chemically activated sample achieved the removal percentage of approximately 99% with the adsorption capacity of 21.460 $mg \cdot g^{-1}$ during the same time, and with longer time, complete removal was obtained. Finally, this study successfully demonstrated a practical method for improving magnetic, microstructural, and adsorptive properties of simple and cost-effective mechano-thermally synthesized zinc ferrite and possibly other ferrites that typically exhibit weak and insufficient adsorptive characteristics.

References

[1] Z.K. Karakaş, R. Boncukcuoğlu, and İ.H. Karakaş, Adsorptive properties of As(III) from aqueous solution using magnetic nickel ferrite ($NiFe_2O_4$) nanoparticles: Isotherm and kinetic studies, *Sep. Sci. Technol.*, 52(2017), No. 1, p. 21.

[2] K.S.M. Abdul, S.S. Jayasinghe, E.P.S. Chandana, C. Jayasumana, and P.M.C.S. De Silva, Arsenic and human health effects: A review, *Environ. Toxicol. Pharmacol.*, 40(2015), No. 3, p. 828.

[3] A.E. Burakov, E.V Galunin, I.V Burakova, A.E. Kucherova, S. Agarwal, A.G. Tkachev, and V.K. Gupta, Adsorption of heavy metals on conventional and nanostructured materials for wastewater treatment purposes: A review, *Ecotoxicol. Environ. Saf.*, 148(2018), p. 702.

[4] J. Gómez-Pastora, E. Bringas, and I. Ortiz, Recent progress and future challenges on the use of high performance magnetic nano-adsorbents in environmental applications, *Chem. Eng. J.*, 256(2014), p. 187.

[5] Y.J. Tu, T.S. Chan, H.W. Tu, S.L. Wang, C.F. You, and C.K. Chang, Rapid and efficient removal/recovery of molybdenum onto $ZnFe_2O_4$ nanoparticles, *Chemosphere*, 148(2016), p. 452.

[6] J.G. Parsons, M.L. Lopez, J.R. Peralta-Videa, and J.L. Gardea-Torresdey, Determination of arsenic(III) and arsenic(V) binding to microwave assisted hydrothermal synthetically prepared Fe_3O_4, Mn_3O_4, and $MnFe_2O_4$ nanoadsorbents, *Microchem. J.*, 91(2009), No. 1, p. 100.

[7] S. Martinez-Vargas, A.I. Martínez, E.E. Hernández-Beteta,

O.F. Mijangos-Ricardez, V. Vázquez-Hipólito, C. Patiño-Carachure, and J. López-Luna, As(III) and As(V) adsorption on manganese ferrite nanoparticles, *J. Mol. Struct.*, 1154(2018), p. 524.

[8] S. Martinez-Vargas, A.I. Martínez, E.E. Hernández-Beteta, O.F. Mijangos-Ricardez, V. Vázquez-Hipólito, C. Patiño-Carachure, H. Hernandez-Flores, and J. López-Luna, Arsenic adsorption on cobalt and manganese ferrite nanoparticles, *J. Mater. Sci.*, 52(2017), p. 6205.

[9] P. Druska, U. Steinike, and V. Šepelák, Surface structure of mechanically activated and of mechanosynthesized zinc ferrite, *J. Solid State Chem.*, 146(1999), No. 1, p. 13.

[10] J. Hu, I.M.C. Lo, and G.H. Chen, Comparative study of various magnetic nanoparticles for Cr(VI) removal, *Sep. Purif. Technol.*, 56(2007), No. 3, p. 249.

[11] J.N. Dui, G.Y. Zhu, and S.M. Zhou, Facile and economical synthesis of large hollow ferrites and their applications in adsorption for As(V) and Cr(VI), *ACS Appl. Mater. Interfaces*, 5(2013), No. 20, p. 10081.

[12] M.P. Reddy, A.M.A. Mohamed, X.B. Zhou, S. Du, and Q. Huang, A facile hydrothermal synthesis, characterization and magnetic properties of mesoporous $CoFe_2O_4$ nanospheres, *J. Magn. Magn. Mater.*, 388(2015), p. 40.

[13] C.G. Anchieta, E.C. Severo, C. Rigo, M.A. Mazutti, R.C. Kuhn, E.I. Muller, E.M.M. Flores, R.F.P.M. Moreira, and E.L. Foletto, Rapid and facile preparation of zinc ferrite ($ZnFe_2O_4$) oxide by microwave-solvothermal technique and its catalytic activity in heterogeneous photo-Fenton reaction, *Mater. Chem. Phys.*, 160(2015), p. 141.

[14] M. Hosseinzadeh, S.A.S. Ebrahimi, S. Raygan, and S.M. Masoudpanah, Removal of cadmium and lead ions from aqueous solution by nanocrystalline magnetite through mechanochemical activation, *J. Ultrafine Grained Nanostruct. Mater.*, 49(2016), No. 2, p. 72.

[15] S. Rajput, C.U. Pittman Jr, and D. Mohan, Magnetic magnetite (Fe_3O_4) nanoparticle synthesis and applications for lead (Pb^{2+}) and chromium (Cr^{6+}) removal from water, *J. Colloid Interface Sci.*, 468(2016), p. 334.

[16] Y.F. Shen, J. Tang, Z.H. Nie, Y.D. Wang, Y. Ren, and L. Zuo, Preparation and application of magnetic Fe_3O_4 nanoparticles for wastewater purification, *Sep. Purif. Technol.*, 68(2009), No. 3, p. 312.

[17] L. Santona, P. Castaldi, and P. Melis, Evaluation of the interaction mechanisms between red muds and heavy metals, *J. Hazard. Mater.*, 136(2006), No. 2, p. 324.

[18] M.K. Sahu, S. Mandal, S.S. Dash, P. Badhai, and R.K. Patel, Removal of Pb(II) from aqueous solution by acid activated red mud, *J. Environ. Chem. Eng.*, 1(2013), No. 4, p. 1315.

[19] S. Sushil and V.S. Batra, Catalytic applications of red mud, an aluminium industry waste: A review, *Appl. Catal. B*, 81(2008), No. 1-2, p. 64.

[20] J.C. Hunter, Preparation of a new crystal form of manganese dioxide: λ-MnO_2, *J. Solid State Chem.*, 39(1981), No. 2, p. 142.

[21] Y.J. Tu, C.F. You, C.K. Chang, and S.L. Wang, XANES evidence of arsenate removal from water with magnetic ferrite, *J. Environ. Manage.*, 120(2013), p. 114.

[22] Y.J. Tu, C.F. You, C.K. Chang, S.L. Wang, and T.S. Chan, Arsenate adsorption from water using a novel fabricated copper ferrite, *Chem. Eng. J.*, 198-199(2012), p. 440.

[23] G.K. Williamson and W.H. Hall, X-ray line broadening from filed aluminium and wolfram, *Acta Metall.*, 1(1953), No. 1, p. 22.

[24] A. Hajalilou, M. Hashim, R. Ebrahimi-Kahrizsangi, H.M. Kamari, and N. Sarami, Synthesis and structural characterization of nano-sized nickel ferrite obtained by mechanochemical process, *Ceram. Int.*, 40(2014), No. 4, p. 5881.

[25] G.F. Goya and H.R. Rechenberg, Ionic disorder and Néel temperature in $ZnFe_2O_4$ nanoparticles, *J. Magn. Magn. Mater.*, 196-197(1999), p. 191.

[26] S. Bid and S.K. Pradhan, Preparation of zinc ferrite by high-energy ball-milling and microstructure characterization by Rietveld's analysis, *Mater. Chem. Phys.*, 82(2003), No. 1, p. 27.

[27] S. Kleiner, F. Bertocco, F.A. Khalid, and O. Beffort, Decomposition of process control agent during mechanical milling and its influence on displacement reactions in the Al–TiO_2 system, *Mater. Chem. Phys.*, 89(2005), No. 2-3, p. 362.

[28] S.H. Zhang, R.X. Shi, and Y. Tan, Comparison of the solubility of $ZnFe_2O_4$, Fe_3O_4 and Fe_2O_3 in high temperature water, *J. Solution Chem.*, 47(2018), p. 1112.

[29] R.A. Shawabkeh, Hydrometallurgical extraction of zinc from Jordanian electric arc furnace dust, *Hydrometallurgy*, 104(2010), No. 1, p. 61.

[30] J. Hu, I.M.C. Lo, and G.H. Chen, Fast removal and recovery of Cr(VI) using surface-modified jacobsite ($MnFe_2O_4$) nanoparticles, *Langmuir*, 21(2005), No. 24, p. 11173.

[31] S.S. Mandaokar, D.M. Dharmadhikari, and S.S. Dara, Retrieval of heavy metal ions from solution via ferritisation, *Environ. Pollut.*, 83(1994), No. 3, p. 277.

[32] G.S. Shahane, A. Kumar, M. Arora, R.P. Pant, and K. Lal, Synthesis and characterization of Ni–Zn ferrite nanoparticles, *J. Magn. Magn. Mater.*, 322(2010), No. 8, p. 1015.

[33] D.W. Green and R.H. Perry, *Perry's Chemical Engineers' Handbook*, 8th Ed., McGraw-Hill, New York, 2007.

[34] Q.L. Li, Y.F. Wang, and C.B. Chang, Study of Cu, Co, Mn and La doped NiZn ferrite nanorods synthesized by the coprecipitation method, *J. Alloys Compd.*, 505(2010), No. 2, p. 523.

[35] A. Gajović, S. Šturm, B. Jančar, A. Šantić, K. Žagar, and M. Čeh, The synthesis of pure - phase bismuth ferrite in the Bi–Fe–O system under hydrothermal conditions without a mineralizer, *J. Am. Ceram. Soc.*, 93(2010), No. 10, p. 3173.

[36] M. Hua, S.J. Zhang, B.C. Pan, W.M. Zhang, L. Lv, and Q.X. Zhang, Heavy metal removal from water/wastewater by nanosized metal oxides: A review, *J. Hazard. Mater.*, 211-212(2012), p. 317.

[37] D. Mohan and C.U. Pittman Jr, Arsenic removal from water/wastewater using adsorbents—A critical review, *J. Hazard. Mater.*, 142(2007), No. 1-2, p. 1.

[38] D. Choi, G.E. Blomgren, and P.N. Kumta, Fast and revers-

ible surface redox reaction in nanocrystalline vanadium nitride supercapacitors, *Adv. Mater.*, 18(2006), No. 9, p. 1178.

[39] S. Mustafa, M.I. Zaman, R. Gul, and S. Khan, Effect of Ni^{2+} loading on the mechanism of phosphate anion sorption by iron hydroxide, *Sep. Purif. Technol.*, 59(2008), No. 1, p. 108.

[40] R. Kefirov, E. Ivanova, K. Hadjiivanov, S. Dzwigaj, and M. Che, FTIR characterization of Fe^{3+}–OH groups in Fe–H–BEA zeolite: Interaction with CO and NO, *Catal. Lett.*, 125(2008), p. 209.

[41] G. Mariani, M. Fabbri, F. Negrini, and P.L. Ribani, High-gradient magnetic separation of pollutant from wastewaters using permanent magnets, *Sep. Purif. Technol.*, 72(2010), No. 2, p. 147.

[42] S.D. Shenoy, P.A. Joy, and M.R. Anantharaman, Effect of mechanical milling on the structural, magnetic and dielectric properties of coprecipitated ultrafine zinc ferrite, *J. Magn. Magn. Mater.*, 269(2004), No. 2, p. 217.

[43] C.N. Chinnasamy, A. Narayanasamy, N. Ponpandian, K. Chattopadhyay, H. Guérault, and J.M. Greneche, Magnetic properties of nanostructured ferrimagnetic zinc ferrite, *J. Phys. Condens. Matter*, 12(2000), No. 35, p. 7795.

[44] M.H. Cao, T.F. Liu, S. Gao, G.B. Sun, X.L. Wu, C.W. Hu, and Z.L. Wang, Single-crystal dendritic micro-pines of magnetic α-Fe_2O_3: Large-scale synthesis, formation mechanism, and properties, *Angew. Chem. Int. Ed.*, 44(2005), No. 27, p. 4197.

[45] M. Ahmadzadeh, A. Ataie, and E. Mostafavi, The effects of mechanical activation energy on the solid-state synthesis process of $BiFeO_3$, *J. Alloys Compd.*, 622(2015), p. 548.

[46] E. Murad, Magnetic properties of microcrystalline iron(III) oxides and related materials as reflected in their Mössbauer spectra, *Phys. Chem. Miner.*, 23(1996), p. 248.

[47] M. Atif, S.K. Hasanain, and M. Nadeem, Magnetization of sol–gel prepared zinc ferrite nanoparticles: Effects of inversion and particle size, *Solid State Commun.*, 138(2006), No. 8, p. 416.

[48] G. Limousin, J.P. Gaudet, L. Charlet, S. Szenknect, V. Barthès, and M. Krimissa, Sorption isotherms: A review on physical bases, modeling and measurement, *Appl. Geochem.*, 22(2007), No. 2, p. 249.

[49] K. Verburg and P. Baveye, Hysteresis in the binary exchange of cations on 2:1 clay minerals: A critical review, *Clays Clay Miner.*, 42(1994), p. 207.

[50] S.X. Zhang, H.Y. Niu, Y.Q. Cai, X.L. Zhao, and Y.L. Shi, Arsenite and arsenate adsorption on coprecipitated bimetal oxide magnetic nanomaterials: $MnFe_2O_4$ and $CoFe_2O_4$, *Chem. Eng. J.*, 158(2010), No. 3, p. 599.

[51] M. Benavente, L. Moreno, and J. Martinez, Sorption of heavy metals from gold mining wastewater using chitosan, *J. Taiwan Inst. Chem. Eng.*, 42(2011), No. 6, p. 976.